Journal of Computational Physics 228 (2009) 5111–5128

Contents lists available at ScienceDirect

Journal of Computational Physics

journal homepage: www.elsevier.com/locate/jcp

A multiple flux boundary element method applied to the description of surface water waves

C.H. Hague, C. Swan *

Department of Civil and Environmental Engineering, Imperial College London, London SW7 2AZ, UK

ARTICLE INFO

Article history:
Received 5 June 2007
Received in revised form 4 March 2009
Accepted 6 April 2009
Available online 22 April 2009

Keywords:
Boundary element method
Multiple fluxes
Corner problem
Free surface waves
Numerical wave tank

ABSTRACT

This paper concerns a two dimensional numerical model based on a high-order boundary element method with fully nonlinear free surface boundary conditions. Multiple fluxes are applied as a method of removing the so-called "corner problem", whereby the direction of the outward normal at geometric discontinuities is ill-defined. In the present method, both fluxes associated with differing directions of the outward normal at a corner are considered, allowing a single node to be placed at that position. This prevents any loss of information at what can be an important part of the boundary, especially if considering simulations of wave reflection and wave run-up. The method is compared to both the double node approach and the use of discontinuous elements and is shown to be a more accurate technique. The success of the method is further demonstrated by its ability to accurately simulate various problems involving wave transmission and wave-structure interactions at domain corners; the results being achieved without the need for filtering, smoothing or re-gridding of any kind.

1. Introduction

Following the first application of a boundary integral approach to the simulation of free surface fluid flows by Longuet-Higgins and Cokelet [1], boundary element methods (BEM) have been increasingly successful in modelling surface water waves. Most recent advances have concentrated on the use of a BEM approach in the context of a "numerical wave tank", whereby waves are generated and absorbed within a closed domain in physical space. By choosing to define the domain in real-space, rather than conformally mapping the free surface, there are no requirements such as the periodicity of the problem or uniform depth. However, one unfortunate consequence of a real-space domain is the presence of discontinuous boundary intersections, commonly termed "corners". At these corners the direction of the outward normal vector to the boundary is undefined, leading to inaccuracies and the build up of numerical errors within a time-marched simulation. Unfortunately the formulation of a BEM, involving repeated integration around the boundaries of the domain, is such that errors arising at the corners will not remain local but will rapidly evolve throughout the computational domain.

In the context of BEM-based wave models, two approaches have traditionally been applied to overcome the corner problem. The first, termed the double node approach, is to specify two nodes at the corner such that they share exactly the same position; one node being associated with each element which makes up the corner. Much work using this technique has been undertaken, some notable examples for two dimensional problems including Grilli et al. [2], Grilli and Svendsen [3], Grilli and Subramanya [4] and Grilli and Horillo [5]. Whilst the double node technique allows for information to be obtained at the corner position itself (important when considering wave-structure interactions, for example), compatibility of

* Corresponding author. Tel.: +44 0 2075945999; fax: +44 0 2075945991.
E-mail address: c.swan@imperial.ac.uk (C. Swan).

0021-9991/$ - see front matter © 2009 Elsevier Inc. All rights reserved.
doi:10.1016/j.jcp.2009.04.012

attributes such as the potential and the velocity between the two nodes must be explicitly enforced. An alternative approach, not as widely used for numerical wave simulations, is to specify discontinuous elements at the domain corners. Within these discontinuous elements the functional representation is usually linear and the nodes which would be placed at the corner are instead moved a short distance inside the element, away from the discontinuity. Although this avoids many of the resulting problems, the interaction at the corner itself is not rigorously examined and therefore important effects may be lost.

This paper investigates the use of multiple fluxes (first outlined for general potential problems in a text by Brebbia and Dominguez [6]) as an alternative way to overcome the corner problem. Section 2 provides a brief outline of the mathematical formulation. This forms the basis of the numerical implementation described in Section 3, with particular emphasis being placed on the description of the corners and the application of the multiple flux representation. Section 4 demonstrates the success of the method via a wide-ranging set of examples including large amplitude standing waves, transmission through an open boundary and wave run-up on a vertical wall. The paper concludes in Section 5 with comments on the benefits of the proposed scheme and the opportunities it affords.

2. Mathematical formulation

2.1. Governing equations

Within the domain Ω, defined in Fig. 1, the flow is considered to be inviscid and irrotational. Accordingly, it can be described by a velocity potential $\phi(x,z,t)$ with a velocity field given by $\mathbf{u} = \nabla\phi = (u,w)$, where the Cartesian co-ordinates (x,z) are again defined in Fig. 1. Mass conservation, which must be satisfied throughout the domain Ω, is then described by Laplace's equation

$$\nabla^2\phi = 0 \quad \text{in } \Omega. \tag{1}$$

Taking the free space Green's function $G(r) = -\frac{1}{2\pi}\ln(r)$, which is a fundamental solution to Laplace's equation, Green's 2nd identity gives the boundary integral equation (BIE) as

$$c_p\phi_p = \int_\Gamma \left[G(r)\frac{\partial\phi_q}{\partial n} - \phi_q\frac{\partial G(r)}{\partial n}\right]d\Gamma. \tag{2}$$

This relates the velocity potential at a point p to the potentials and potential fluxes at points q around the boundary Γ. The distance between points p and q is given by $r = |\mathbf{x}_p - \mathbf{x}_q|$, where $\mathbf{x}_p = (x_p, z_p)$ and $\mathbf{x}_q = (x_q, z_q)$ are the position vectors of the points, $\mathbf{n}$ is the unit outward normal vector, and c_p is a geometric coefficient. Within this paper, a rigid mode technique is used in order to avoid the explicit calculation of c_p. Further details concerning the derivation and application of Eq. (2) are given in [6].

The movement of the free surface, Γ_s, must satisfy both the kinematic and dynamic free surface boundary conditions (KFSBC and DFSBC); the former ensuring that the water surface is a streamline, and the latter that the pressure on the water surface remains constant. In a semi-Lagrangian frame, allowing the surface points to move vertically but not horizontally, these conditions are described in [7] as

$$\frac{\delta\eta}{\delta t} = \frac{\partial\phi}{\partial z} - \frac{\partial\phi}{\partial x}\frac{\partial\eta}{\partial x}, \tag{3}$$

$$\frac{\delta\phi}{\delta t} = -g\eta - \frac{1}{2}\left[\left(\frac{\partial\phi}{\partial x}\right)^2 + \left(\frac{\partial\phi}{\partial z}\right)^2\right] + \frac{\partial\phi}{\partial z}\frac{\delta\eta}{\delta t}; \tag{4}$$

the differential operator δ being chosen to represent the semi-Lagrangian nature of the formulation and defined by $\delta/\delta t = \partial/\partial t + w\partial/\partial z$. Alternatively, in a Lagrangian frame whereby points on the free surface are free to follow the fluid the KFSBC and DFSBC are given in [1] as

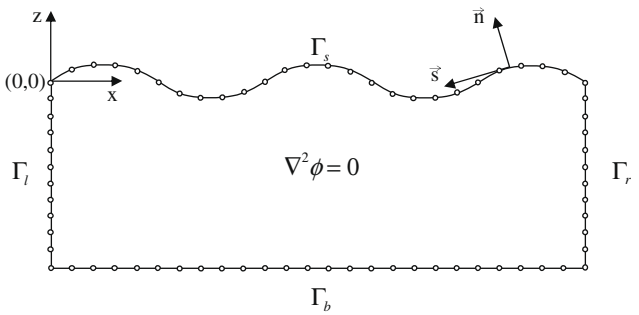

Fig. 1. General domain used for computations. The boundary is composed of sections $\Gamma_b, \Gamma_r, \Gamma_s$ and Γ_l, along which integrations are carried out in an anticlockwise direction, indicated by the tangential vector $\vec{s}$. This ensures the normal vector $\vec{n}$ is always directed outwards from the domain.

$$\frac{D\eta}{Dt} = \frac{\partial \phi}{\partial z}, \tag{5}$$

$$\frac{D\phi}{Dt} = -g\eta + \frac{1}{2}\left[\left(\frac{\partial \phi}{\partial x}\right)^2 + \left(\frac{\partial \phi}{\partial z}\right)^2\right], \tag{6}$$

where D/Dt is the material derivative, defined by $D/Dt = \partial/\partial t + u\partial/\partial x + w\partial/\partial z$.

2.2. Boundary conditions appropriate to the numerical domain

The potential on the free surface, Γ_s, is specified as a Dirichlet-type boundary condition such that

$$\phi = \phi|_{known} \quad \text{on } \Gamma_s, \tag{7}$$

and is usually given an initial value appropriate to still water conditions such that $\phi = 0$ at $t = t_0$. At later times $\phi(t > t_0)$ is obtained by time-marching the free surface boundary conditions.

The boundary conditions imposed along the other sections of the domain are specified as follows. The bed, Γ_b, is impermeable and thus the potential flux is taken to be zero

$$\frac{\partial \phi}{\partial n} = 0 \quad \text{on } \Gamma_b. \tag{8}$$

Neumann-type conditions are also specified on the lateral boundaries of the domain, Γ_l and Γ_r, taking the form of known values or reflective walls, depending on the problem to be solved,

$$\frac{\partial \phi}{\partial n} = \left.\frac{\partial \phi}{\partial n}\right|_{known} \quad \text{or} \quad \frac{\partial \phi}{\partial n} = 0 \quad \text{on } \Gamma_l, \Gamma_r. \tag{9}$$

Eqs. (7)–(9) define a mixed boundary condition problem for which the solution of Eq. (2) gives ϕ on Γ_b, Γ_l and Γ_r and $\partial\phi/\partial n$ along Γ_s. By combining this latter information with the variation of ϕ in the tangential direction, $\partial\phi/\partial s$, the velocities $u = \partial\phi/\partial x$ and $w = \partial\phi/\partial z$ can be obtained. These velocities are then substituted into Eqs. (3) and (4) or (5) and (6), depending on the frame of reference being used, and the free surface boundary conditions integrated with respect to time. For the first three steps this time integration is undertaken using a fourth-order Runge–Kutta scheme. Beyond this, sufficient information is available to adopt an Adams–Bashforth–Moulton predictor–corrector scheme with a fifth-order corrector step being used in conjunction with a fourth-order predictor; details of this approach being given in [8].

3. Numerical implementation

The purpose of the numerical solution is to solve the BIE (2) at a given number, N, of positions around the boundary of the domain in order to find the N unknown potential or potential fluxes at these positions. Although this aim is shared by both the double node approach and the multiple flux technique, there are some subtle yet important differences between the two.

3.1. Differences between multiple fluxes and double nodes

In order to solve the N unknowns, corresponding to the N positions of interest around a four-cornered domain (Fig. 1), the double node method specifies a total of $N + 4$ nodes; the four additional nodes appearing due to the extra node required at each corner. Applying the BIE (2) at each node gives rise to $N + 4$ simultaneous equations. In a physical sense there remain only N unknowns, corresponding to either one potential or one potential flux at each spatial location. However, with the implementation of double nodes four additional "unknowns" are introduced and these must be solved in a way that ensures that the two nodes representing each double node remain collocated and that the solution is physically realistic at these nodes. As a minimum this requires the imposition of additional constraints to ensure continuity of the potential values, so that points with the same co-ordinates have an identical potential. In practice, constraints are also imposed to ensure the compatibility of the potential fluxes so that the velocity vector is uniquely defined at both corner (double) nodes. An alternative way of describing this situation (following Grilli and Svendsen [3]) is to acknowledge the physical reality at these corner points and to argue that with $N + 4$ simultaneous equations and N (genuine) unknowns, the problem is over-determined and the corresponding system matrix poorly conditioned (theoretically singular). As a result, the double node approach requires this over-determination to be removed by explicitly imposing continuity and compatibility conditions.

Irrespective of how it is described, it is clear that the application of a double node approach requires the imposition of additional constraints; these constraints having become increasingly sophisticated for both 2D domains (e.g. [2–5]) and 3D domains (e.g. [9,10]). In the first instance, the continuity of potential at each double node requires $\phi_a = \phi_b$, where the subscripts a and b correspond to the two parts of the double node. This condition is relevant to corners involving both Dirichlet–Neumann and Neumann–Neumann boundary conditions. An obvious way of achieving this is to specify the change directly within the matrix formulation and to remove entirely the relevant BIE (2) thereby reducing the size of the system matrix by one (per double node). However, it is argued by Grilli and Svendsen [3] that this would be computationally

expensive. As a result, the relevant entry is replaced by a condition that following the matrix solution yields $\phi_a = \phi_b$. Unfortunately, since the matrix solution will never be exact, small errors will persist in this important condition. In many cases this may be unimportant. Nevertheless, it is widely acknowledged (not least by Grilli and Svendsen [3]) that, with no damping in the model, small numerical errors may add up through time sometimes leading to an instability in the solution.

More importantly, the imposition of the compatibility conditions is also relevant to the solution of corners involving Dirichlet–Neumann boundary conditions. Since, in the present context, these involve an intersection with the water surface, they are particularly troublesome. Specifically, they set out to calculate the velocity vector at the corner associated with the free surface element using the calculated normal derivative, $\partial\phi/\partial n$, and the tangential gradient of the 'known' surface potentials, $\partial\phi/\partial s$. Following the solution of the system matrix, these calculations are employed to make an *a posteriori* correction to ensure compatibility of the velocity vector either side of the corner. Unfortunately, the accuracy of the s-derivative is difficult to maintain as a corner is approached because with the use of sliding polynomials [2] they are based more on extrapolation than interpolation [3]. In such cases the growth of corner instabilities, as noted above, may again become an issue.

Indeed, such difficulties have been the subject of considerable investigation leading to a system of extended compatibility conditions [11,4] in which a related set of equations are applied *a priori*. In this case the potential at the free surface corner node is treated as an unknown rather than a boundary condition and calculated as part of the system solution in order to satisfy the required compatibility constraint. Although this latter approach is shown to provide improved solutions [4] when used with the specified combination of linear shape functions to discretise the field variables and cubic splines to reproduce the geometry, the difference between these implementations confirms the dependence of the double node solutions on the nature of the applied continuity and compatibility conditions.

In contrast, the multiple flux method employs no such additional constraints, either continuity or compatibility. With the adoption of quadratic elements, each element has three nodes. The problem therefore becomes one in which there are N positions (or nodes) around a boundary discretised into M elements. Three fluxes are specified per element, with adjacent elements sharing an end node, but not necessarily the same flux. This results in an intermediate description of the domain as consisting of $3M$ fluxes, N nodes and N potentials. On those parts of the boundary that are smooth, the two fluxes are considered to be identical, whereas at domain corners they are considered to be different and are treated separately. Manipulation of this intermediate matrix system is undertaken using a swapping procedure, full details of which are given in the next section. The key point to note is that this manipulation involves neither the introduction of new constraints nor the removal of any information from the matrix solution; it simply involves the rearrangement of knowns and unknowns and seeks to place the coefficients that act on identical fluxes into the same matrix elements. Once complete, this results in an algebraic system of N simultaneous equations which is exactly consistent with the number of unknowns. As such, no over-determination arises and the solution can progress as below.

3.2. Discretisation of the boundary

As noted above, to evaluate the BIE (2), N nodes are placed around the boundary to form M isoparametric quadratic elements, where $N = 2M$ since nodes joining elements are shared. Each element is mapped onto a reference element with intrinsic coordinate ξ, and both the geometry and variables along an element can then be described by shape functions, $\mathcal{N}_c(\xi)$, such that

$$s(\xi) = \sum_{c=1}^{3} \mathcal{N}_c(\xi) s_c, \tag{10}$$

where $s(\xi)$ can be any of x, z, ϕ, or $\partial\phi/\partial n$. The integration across elements is carried out using Gauss quadrature and the BIE arranged in a matrix formulation

$$\mathbf{H\Phi} = \mathbf{G\Phi}_n, \tag{11}$$

where the arrays **H** and **G** contain coefficients which multiply both known and unknown nodal values of potential and potential flux around the boundary. Now, as previously mentioned, the corner problem exists where the domain boundary ceases to be smoothly varying, at points where the geometry of the boundary forms a corner. At these positions the outward normal, and hence the outward flux $\partial\phi/\partial n$, is no longer well-defined. However, the elements which meet at the corner have a variation of flux associated with the shape functions specified along that element (see Fig. 2). By keeping each of these fluxes in the solution step and considering them to be both valid at the corner, an accurate representation of the behaviour at the corner can be achieved.

Multiple fluxes are considered to exist at all nodes where elements meet, one flux for each element connecting at that point and with a direction associated with the outward normal of that element. In this way, integrations are carried out such that the contributions due to each of these fluxes is considered to be separate. Therefore, although **H** is of size $N \times N$ since there can only be one value for potential at each node, the matrix **G** is rectangular of size $N \times 3M$ and the vector $\mathbf{\Phi}_n$ is of length $3M$.

In deriving a solution, Eq. (11) can then be transformed to a system matrix formulation

$$\mathbf{AX} = \mathbf{B}, \tag{12}$$

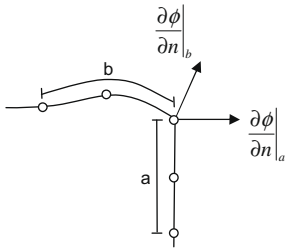

Fig. 2. Multiple fluxes at a corner.

where **A** is the system matrix (size $N \times N$), **X** is a vector of size N containing the unknowns (a mixture of fluxes and potentials), and **B** is an array of known values (size N). This is achieved by means of certain swapping routines. These routines either swap the coefficients in **H** and **G**, absorb them into the system matrix **A**, or retain them to multiply known boundary values to form **B**. At this stage, it is important to note that in transforming equations (11) to (12) nothing is removed from the system formulation or modified in any way. Specifically, there is no reduction in the number of unknowns, no lines of the matrix formulation (corresponding to the implementation of the BIE (2)) are removed, and no additional constraints are imposed. As a result, this manipulation is very different to that which is adopted in a double node solution. Indeed, as mentioned in the previous section, the aim of the swapping routines is simply to rearrange the knowns and unknowns and to place coefficients that act on identical fluxes into the same matrix elements. Once this is achieved, the dot product of **G** and $\mathbf{\Phi}_n$ automatically results in a vector of knowns **B** which is of length N, thus producing a system of N simultaneous equations for N unknowns. Most importantly, this is achieved by considering all the fluxes ($3M$ in total) around the boundary.

The procedure necessary to achieve this manipulation is as outlined by Brebbia and Dominguez [6] and can be summarised as follows. Around the boundary of the domain, there will be $3M$ specified boundary conditions denoted by ($j = 1, 3M$), each corresponding to a node ($i = 1, N$). Depending on the nature of these conditions the columns of **H** and **G**,which contain all the instances (in every BIE) where coefficients act on a particular known or unknown, are swapped according to the following rules:

- *At an element mid-point*
  - If condition j involves a specified flux, $\partial\phi/\partial n$, no change should be made. In this way, the single known flux is kept on the right hand side of the system formulation.
  - If condition j involves a specified potential, ϕ, swap column i of **H** with column j of **G**, reversing the sign of column entries. This moves the known potential to the right hand side of the system formulation and ensures that coefficients which multiply the unknown flux are placed in the system matrix.

- *At a junction between two elements*
  - If condition j involves $\partial\phi/\partial n$ and condition $j+1$ also involves $\partial\phi/\partial n$, no change should be made. In this way, all fluxes which are known are treated separately on the right hand side of the system formulation. This type of junction is present at a Neumann–Neumann corner, whereby the potential fluxes are given as boundary conditions either side of the corner and the only unknown is the potential at the corner node.
  - If condition j involves $\partial\phi/\partial n$ and condition $j+1$ involves ϕ, column i of **H** and column $j+1$ of **G** are swapped with a reversal of sign. Column j of **G** is therefore left in place, containing coefficients associated with the known flux, whilst column $j+1$ now contains coefficients associated with the known potential. This leaves the unknown flux on the left hand side of the system formulation. This type of junction occurs at a Dirichlet–Neumann corner, whereby the potential is specified at the corner node and the potential flux corresponding to one of the elements making up the corner is given as a boundary condition. The unknown is then the flux corresponding to the other element that completes the corner. In the case of a corner on the free surface, this is the flux associated with the unknown fluid velocity on the surface.
  - If condition j involves ϕ and condition $j+1$ also involves ϕ, swap column i of **H** with column j of **G**, reversing the sign of column entries, then add column $j+1$ of **G** (after a reversal of sign) to column i of **H**. Set column $j+1$ of **G** to 0. By doing this, the two unknown fluxes are considered to be identical, and thus any coefficients which act on the same unknown are absorbed into the system matrix. This type of junction occurs along the free surface, where the domain is smoothly varying.

After the swapping procedure is completed, the vector $\mathbf{\Phi}_n$ contains only known values and **G** contains the coefficients which act on these knowns, the dot product of these two arrays producing the vector **B**. The matrix **H** contains coefficients which act on the system unknowns and, as such, becomes the system matrix **A**. Eq. (12) is then solved for **X**. This can be undertaken by direct Lower–Upper decomposition. However, for reasons of computational efficiency, a GMRES algorithm [12] is used in the present study to solve for the vector **X**.

3.3. Restrictions on the types of corner at which multiple fluxes can be applied

Following the explanation of the swapping procedure for junctions between elements, it is clear that the multiple flux approach is applicable for all corner types except Dirichlet–Dirichlet corners. By allowing multiple fluxes to exist at the corner, either the potential or one of the fluxes can be solved for, but in this case both fluxes are unknown. Unlike the junctions arising along a smoothly varying boundary such as the water surface, these fluxes cannot be assumed to be identical. As a result the two components of the potential flux cannot be solved using the present method. Fortunately, when modelling water waves in the context of what is commonly referred to as a "numerical wave tank", only the first two types of corner are present in the domain. Accordingly, the multiple flux approach is applicable to any numerical problem specified in this way.

3.4. Absorption and radiation of wave energy

In order to prevent any unwanted build up of excess wave energy in the numerical domain a coupled absorption/radiation scheme similar to that of Clement [13] was employed. However, after extensive testing it was found that the performance of the scheme could be much improved by the introduction of an assumed depth dependence. In implementing this coupled scheme, a section of the free surface at the downstream end of the domain, beginning at position x_{sponge} and being of length L_{sponge}, acts as a numerical sponge layer such that the dynamic free surface boundary condition is modified by a damping coefficient μ according to

$$\frac{\delta\phi}{\delta t} = -g\eta - \frac{1}{2}\nabla\phi\nabla\phi + \frac{\partial\phi}{\partial z}\frac{\delta\eta}{\delta t} - \mu\frac{\partial\phi}{\partial n}, \tag{13}$$

where μ is given by

$$\mu = 3\beta\left(\frac{x - x_{sponge}}{L_{sponge}}\right)^2 - 2\beta\left(\frac{x - x_{sponge}}{L_{sponge}}\right)^3 \tag{14}$$

and the damping strength β is chosen to be 0.3.

In addition to this passive damping, the downstream boundary acts according to the Sommerfeld radiation condition, with a depth variation implemented such that the radiated velocity takes the form of the velocity profile $u(z)$ of a linear regular wave. This is achieved as follows: the Sommerfeld radiation condition states that

$$\frac{\partial\phi}{\partial x} = -\frac{1}{c}\frac{\partial\phi}{\partial t}, \tag{15}$$

where c is the phase velocity of the wave and, since the boundary conditions are supplied at each step before the boundary integral solution, the value of $\partial\phi/\partial t$ must be known at the radiation boundary. However, since waves propagate along the free surface in a fully nonlinear sense, this quantity is not known *a priori*. Therefore information that is known upstream of the boundary, coupled with knowledge of the phase velocity c, is used to predict the value of $\partial\phi/\partial t$ at each step. The position upstream, x_{up}, one time step before at which the value of $\partial\phi/\partial t$ satisfies

$$\left.\frac{\partial\phi}{\partial t}\right|_{x,t} = \left.\frac{\partial\phi}{\partial t}\right|_{x_{up},t-\Delta t} \tag{16}$$

is

$$x_{up} = x - c\Delta t, \tag{17}$$

which does not necessarily coincide with the position of a node. Therefore, once the position x_{up} is known, the element within which it exists can be identified and the Eulerian time derivative $\partial\phi/\partial t$ interpolated at that position from nodal values. In this way the radiation condition becomes

$$\frac{\partial\phi}{\partial x} = -\frac{1}{c}\left.\frac{\partial\phi}{\partial t}\right|_{x_{up},t-\Delta t}. \tag{18}$$

This condition only applies to points along the free surface η. In order to provide a depth variation to better mimic the velocity profile of the outgoing wave, a separation of variables approach is adopted in which the horizontal velocity is assumed to have the same form as that of a linear progressive wave. In this case the velocity profile can be considered to consist of two parts, such that

$$u(x,z,t) = \alpha(x,t)\gamma(z), \tag{19}$$

where α is the non-depth dependent part

$$\alpha(x,t) = \frac{ag}{\omega}k\cos(kx - \omega t) \tag{20}$$

and γ describes the depth variation

$$\gamma(z) = \frac{\cosh(k(z+d))}{\sinh(kd)}. \tag{21}$$

The radiation condition (18) is therefore applied for the uppermost node on the boundary which is situated at η, thus giving a horizontal velocity for that node. This is then divided through by γ, setting $z = \eta$. This leaves the non-depth dependent part α_{rad}, given by

$$\alpha_{rad} = \frac{\partial \phi}{\partial x}\gamma(\eta)^{-1} \tag{22}$$

and the boundary condition can then be specified at all depths along the radiation boundary as

$$\frac{\partial \phi}{\partial n}(z) = \alpha_{rad}\gamma(z). \tag{23}$$

By applying Eq. (23) the excessive removal of wave energy at depths below the free surface is avoided and a more realistic boundary condition imposed (compared to the depth-independent Sommerfeld condition usually applied in numerical models).

4. Discussion of results

4.1. Simulation of a large amplitude standing wave (LASW)

This initial test case concerns a large amplitude standing wave (LASW) of height $H = 1.16$ m and wavelength $\lambda = 2\pi$ m, with a corresponding wave steepness of $Hk/2 = 0.58$. The domain length is 2π m$(-\pi \leqslant x \leqslant \pi)$ and the still water depth $d = \pi$ m so that the waves are effectively propagating in deep water, $kd = \pi$. This case has previously been considered by Hamano et al. [14] and was shown to present significant difficulties in terms of the corner problem; evidence of this including both the occurrence of non-physical jetting near the domain boundaries, leading to the eventual break-down of the code, and poor energy conservation. The purpose of the present comparisons is two-fold. First, to demonstrate the ability of the present multiple flux solution to model this challenging case in the physical domain, without imposed periodicity and without the need for smoothing, filtering or re-gridding of any kind. Second, to make direct comparisons with the energy fluctuations presented in [14], demonstrating the superiority of the multiple flux approach when compared to both double nodes and discontinuous elements.

In the present calculations, a total of 100 elements are distributed around the domain, with 31 elements (63 nodes) along the free surface. The initial conditions concern the water surface profile at $t = 0$. In accordance with [14] two examples are considered: the first described as the trough–trough case, in which the crest of the standing wave is initially placed in the center of the domain $(x = 0)$, and the second described as crest–crest, which is phase lagged by $T/2$ and therefore commences with a wave trough at $x = 0$. A time step of $\Delta t = 0.01$ s is used for both examples, and the numerical model is run in a semi-Lagrangian frame. Fig. 3 shows the wave profile at discrete phases of the wave cycle, overlying the results relating to the different starting positions. It can be seen that the nature of the starting profile does not affect the simulation of the free surface evolution. Further evidence of this is given in Fig. 4, which shows the free surface profile at intervals of the wave period, T, for both the crest–crest (plotted from $t = T/2$) and trough–trough starting profiles (plotted from $t = T$). Each of the traces overlie each other almost perfectly. In achieving these results it is important to stress that no filtering, smoothing or re-gridding has been applied.

In their earlier consideration of this problem, Hamano et al. [14] adopted a Lagrangian BEM formulation, both with and without re-gridding, and demonstrated that with double nodes applied to tackle the corner problem, there was a global rise in the total energy present in the domain. Furthermore, comparisons between the double node solution and a high resolution (250 surface nodes) Longuet-Higgins and Cokelet [1] solution, in which the latter assumes periodicity and therefore eliminates entirely the corner problem, show significant departures in the predicted corner geometry. To tackle these problems, Hamano et al. [14] replaced the double nodes at corners with discontinuous elements, in which the corner node is moved inside the element away from the discontinuity. From a physical perspective, this approach is not entirely satisfactory; the reason for this being as follows. Whilst their results confirm that the corner nodes are vitally important to the success of the solution, both physically and computationally, their adopted approach seeks to overcome the inherent difficulties by avoiding a rigorous description of exactly these locations. As far as the present paper is concerned, the key issue lies in the relative merit of the multiple flux approach when compared to the double node technique and the use of discontinuous elements.

In making these comparisons, it is important to note that Hamano et al. used linear elements for their double node model, this being the obvious choice for comparison to the linear discontinuous element model. However, in order to fairly assess the performance of the current multiple flux model when applied to the LASW example, it is necessary to include a higher-order double node model for comparison. Therefore, in addition to the original results presented in [14], a BEM-based model using quadratic isoparametric elements was applied to the problem. This was chosen to be as consistent as possible with the

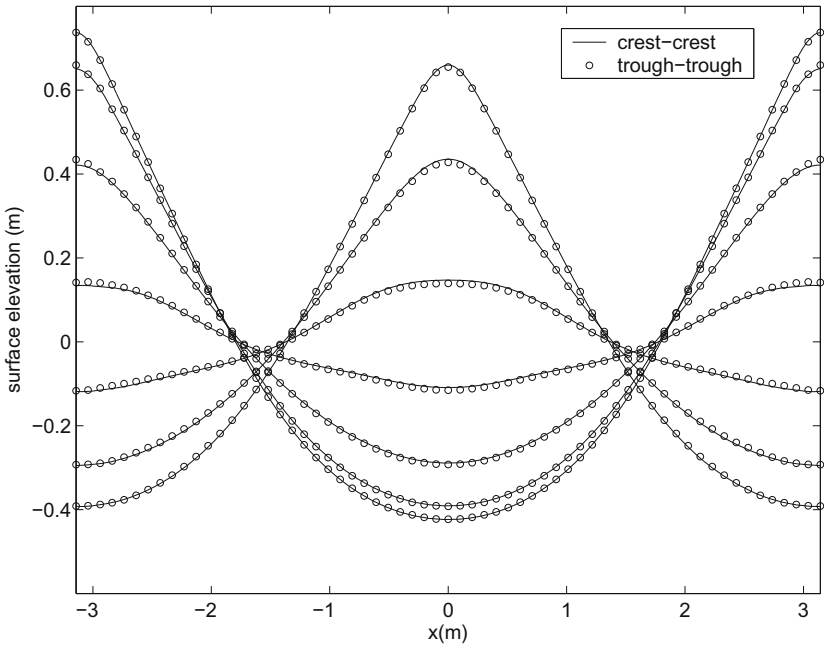

Fig. 3. A large amplitude standing wave at various phases of the wave cycle; comparisons between calculations started from either crest–crest or trough–trough profiles.

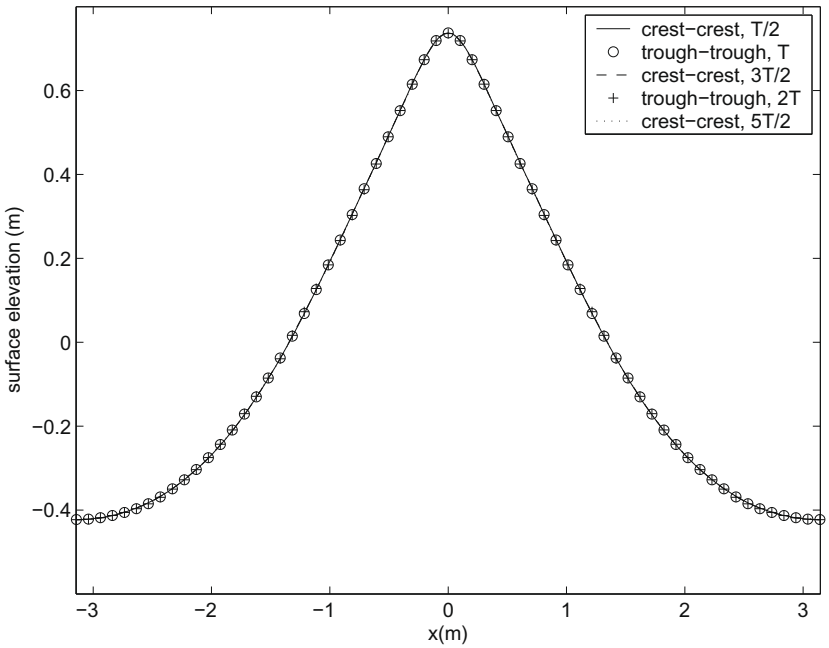

Fig. 4. Large amplitude standing wave: free surface profiles at intervals of the wave period, T, for both crest–crest (plotted from $t = T/2$) and trough–trough (plotted from $t = T$) starting profiles.

current multiple flux model, in order to be confident that differences in results could be attributed solely to the treatment of corners.

At this stage it is relevant to note that more sophisticated double node models have been proposed [11,4] in which extended compatibility conditions are applied *a priori* (see Section 3). However, these have not been considered in the present comparisons for two reasons. Firstly, the introduction of the extended compatibility conditions was, in large part, motivated by the desire to overcome the difficulties associated with moving boundaries. Whilst this undoubtedly represents a very

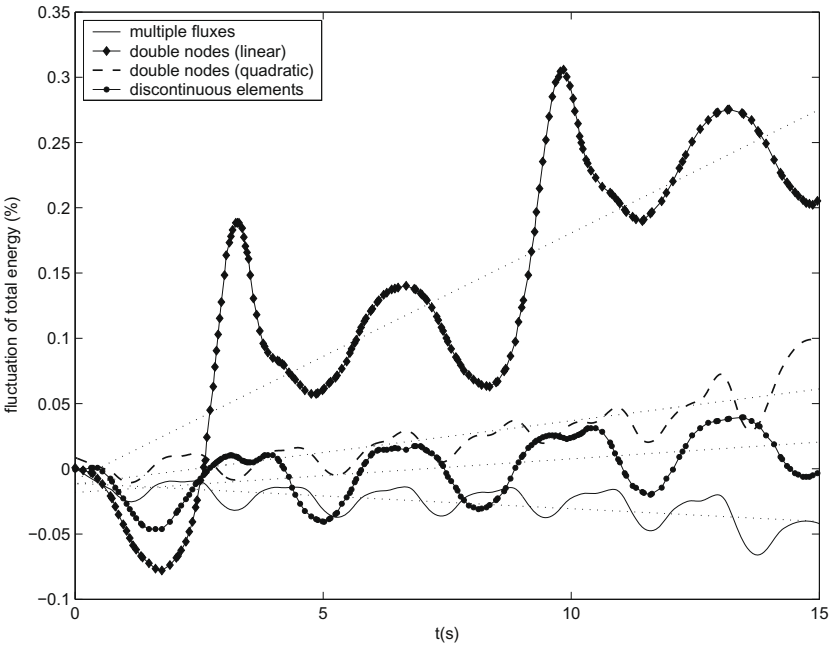

Fig. 5. Large amplitude standing wave: time variation in total energy. Note: dotted lines indicate the mean global energy change over time associated with each method.

important condition, it is not one that has been considered in the present study. Secondly, the success of this approach was shown by Grilli and Subramanya [4] to be, in part, dependent upon the details of both the discretisation of the field variables and the reproduction of the surface geometry; the former being modelled using linear shape functions and the latter cubic splines. Indeed, [4] provide a detailed discussion as to why the extended compatibility conditions appear to give better results when combined with a less accurate (linear) representation of the field variables. Such issues merely serve to complicate and confuse the straightforward comparisons we are seeking to provide between double nodes and multiple fluxes, with all other factors remaining constant.

Accordingly, the double node formulation we have adopted is that outlined in Grilli et al. [2] and employed in Hamano et al. [14] and Baudic et al. [15][1]. Within this model, the continuity of potential and the compatibility of the velocity vector is as described in Section 3.

Within the numerical calculations the total energy across the entire domain (of length L) at each time step can be calculated according to:

$$E(t) = E_k(t) + E_p(t), \tag{24}$$

where the kinetic energy is expressed as

$$E_k(t) = \frac{1}{2}\rho \int_{\Gamma_s} \phi \frac{\partial \phi}{\partial n} d\Gamma \tag{25}$$

and the potential energy is given by

$$E_p(t) = \frac{1}{2}\rho g \int_{x=x_0}^{x=x_L} (\eta(x) + d)^2 dx. \tag{26}$$

Fig. 5 shows the variation of total energy obtained using the multiple flux boundary element method. The results are compared to those obtained in [14] for both the double node technique (linear elements) and discontinuous elements, along with those obtained by applying the double node technique with quadratic elements. Further detailed comparisons of this data are also presented in Table 1 The most obvious point to note from these comparisons is that in terms of energy conservation, the double node approach with linear elements is at least an order of magnitude worse than the use of either discontinuous elements or the multiple flux approach. Whilst the use of quadratic elements in the double node technique greatly improves the situation, the energy fluctuation of the latter remains almost two and a half times that of the multiple flux model.

In considering these results, the average rate of change of energy, $\partial \bar{E}/\partial t$, indicated by the trend lines on Fig. 5, may be taken as a measure of the longer-term stability of the numerical calculations. In this case the multiple flux approach is

[1] The only difference in this latter case being the use of cubic elements rather than quadratic.

Table 1
Energy conservation, a comparison of BEM formulations applied to a large amplitude standing wave. Note: $\Delta E = (E - \bar{E})$ and $()_{mf}$ describes the corresponding value for the multiple flux formulation.

Energy constraint	Model formulation			
	Double nodes (linear)	Double nodes (quadratic)	Discontinuous elements	Multiple fluxes
$\partial\bar{E}/\partial t$	0.0189	0.0049	0.0026	0.0020
$RMS(\Delta E)$	0.0547	0.0129	0.0194	0.0099
$\frac{(\partial\bar{E}/\partial t)}{(\partial\bar{E}/\partial t)_{mf}}$	9.5	2.5	1.3	1.0
$\frac{RMS(\Delta E)}{RMS(\Delta E)_{mf}}$	5.5	1.3	2.0	1.0

the most accurate; the gradient of the next best method, involving discontinuous elements, being 30% larger and the double nodes based on quadratic elements being two and a half times larger (see Table 1). Furthermore, if the root-mean-square fluctuations about the trend lines, $RMS(\Delta E)$ where $\Delta E = (E - \bar{E})$, are taken as a measure of the energy fluctuations within a single wave period, the multiple flux method is again the most accurate; the RMS values relating to double nodes with quadratic elements being around 30% larger than the multiple flux approach and those relating to the model with discontinuous elements being twice as large. This latter result is consistent with the notion that in omitting a rigorous description of the corner points, the cyclic variation in the energy levels would be expected to increase, particularly in those flows where the most nonlinear behaviour or extreme surface elevations arise at the boundary of the domain and therefore directly involve the corner points.

In making the comparisons presented on Fig. 5 and in contrasting the data given in Table 1, it is important to note that the multiple flux method has been compared with 'equivalent' formulations of the double node and discontinuous element approaches; particularly in respect of the order of the element employed. Whilst it is clear that the multiple flux method is preferable, on all counts, this should not be taken as an implied criticism of other methods in which double nodes have been combined with higher-order elements and extended compatibility conditions [4]. Nevertheless, given the success of the multiple flux method (see below), one should question whether these additional levels of complexity are really necessary or whether they simply address a difficulty caused by the adoption of the double node approach.

The LASW simulation also provides an opportunity to consider the convergence of the multiple flux model with varying discretisation. To investigate this, the rate of energy change is again considered, but with varying mesh densities. If the mesh density h is defined such that $h = 1$ corresponds to the original discretisation in space and time, doubling the value of h corresponds to a doubling of the density of the numerical mesh with a corresponding increase in the temporal resolution. This is achieved by halving both the nodal separation and the time step so that $\Delta x_{(h=2)} = \Delta x_{(h=1)}/2, \Delta z_{(h=2)} = \Delta z_{(h=1)}/2$ and $\Delta t_{(h=2)} = \Delta t_{(h=1)}/2$. Fig. 6 shows the dependency of $\partial\bar{E}/\partial t$ on the mesh density, with data based on simulations undertaken

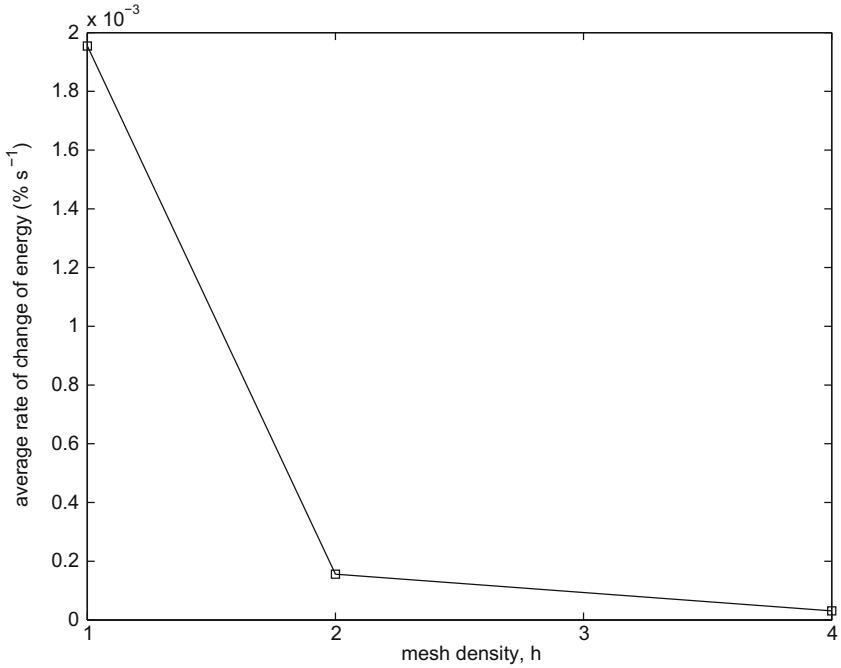

Fig. 6. Dependence of energy error on mesh density for the large amplitude standing wave example.

at $h = 1, 2$ and 4. With increasing levels of discretisation, it can be seen that the energy change rapidly reduces to a very small value, indicating the inherent convergence of the multiple flux method.

Although the energy fluctuations discussed above hint at the difficulties of dealing with the corner problem, they do not perhaps reflect the true extent of the problems arising. For example, in considering this case Hamano et al. [14] argued that the accuracy of the interpolation necessary for re-gridding was one potential source of the energy errors. However, when attempting to run the discontinuous element method without re-gridding, calculations initiated with a central wave crest (the trough–trough case) involved the rapid development of non-physical jetting near the corners, leading to the breakdown of the model within the first half wave period, $t < T/2$. In contrast, calculations initiated with a central wave trough (the crest–crest case) proved more successful. Unfortunately, given the symmetry of the problem in hand, it is unclear why this should be so. In the present study, involving the multiple flux formulation, no such difficulties arise. Indeed, the data presented in Fig. 4 confirm that the large amplitude standing wave perfectly repeats itself, irrespective of the starting position.

4.2. Mass transport through the input corner

When a nonlinear regular wave train propagates in water of constant depth there is a small drift, commonly referred to as the mass transport velocity. This has two components. The first, the so-called Stokes drift, is a depth varying Lagrangian flow which is positive (in the same direction as the phase velocity) at all elevations and arises due to the non-closure of the particle orbits. The second corresponds to an Eulerian backflow. This is uniform with depth, driven by small hydrostatic pressure gradients and necessary to ensure that the combined drift integrated with depth produces zero net transport. At a second-order of wave steepness, this mass transport velocity is given by Dean and Dalrymple [16] as

$$\bar{u}_{drift} = \frac{a^2 \pi k \cosh(2k(d+\eta))}{T \sinh^2(kd)} - \frac{a^2 k \pi \coth(kd)}{Tkd}, \tag{27}$$

where the first term is the Lagrangian Stokes drift and the second the Eulerian return flow.

In the present context, these components of the drift velocity are of interest for two reasons. First, they arise due to small (second-order) differences in the large orbital velocities and, as a consequence, their accurate prediction becomes a significant test of the BEM formulation. Second, the input conditions specified on the left boundary, Γ_I on Fig. 1, are known values of the potential flux (Eq. (9)). With no attempt made to control the vertical position of the corner node on this input boundary, the mass flux through the boundary, corresponding to the drift velocity, is critically dependent on the accurate representation of the corner node and hence the multiple flux method.

Before discussing these results it is important to draw a distinction with earlier work concerning particle trajectories. For example, Grilli and Horillo [5] considered the Lagrangian drift, but only in respect of modifying the required input conditions in order to enable the generation of nonlinear wave forms. In fact, the Lagrangian drift velocity was calculated iteratively and incorporated into the boundary condition as a reverse current so that apparent "non-physical" effects due to the mean mass influx could be avoided. In contrast, the present study will demonstrate that both the Lagrangian drift velocity and the associated Eulerian return flow are accurately generated by the model itself, with no modification of the input conditions; both flows representing real physical effects arising as a consequence of the closed nature of the numerical wave tank. Skourup and Jonsson [17] also calculated some particle trajectories. However, these concern the mean flow or circulation about a horizontal cylinder and do not directly concern either the Stokes drift or the Eulerian return flow. Nevertheless, in considering the zero mean particle velocity which follows directly from their imposed periodic lateral boundary conditions, they acknowledge that "This (zero) net transport of fluid means that our results are not directly comparable with closed flume wave tests". It therefore follows that if the wave-induced mean flows are to be correctly modelled, the corner problem must be effectively tackled.

Within this example, a weakly nonlinear regular wave train of amplitude $a = 0.05$ m and wavelength $\lambda = 1.5$ m is considered so that the calculated components of the drift velocity can be directly compared with a second-order Stokes solution (Eq. (27)). A numerical domain of length $L = 20$ m and depth $d = 1$ m was specified, with the domain boundary discretised into a total of 420 elements. This gives 840 nodes around the boundary, 401 being placed on the free surface; the corresponding spatial discretisation being $\Delta x = \Delta z = 0.05$ m. A time step of $\Delta t = 0.02$ s was adopted and the input velocity ramped up from zero over the first 3 s of the simulation. The coupled damping outlined in Section 3.4 was implemented, with passive damping placed in the final downstream 2 m of the domain.

To first check the wave profile generated by the input boundary, the free surface profile propagating into the domain is compared in Fig. 7 to the analytic Stokes 5th-order solution proposed by Fenton [18]. Part (a) contrasts the time-history of the water surface elevation, $\eta(t)$ at the input boundary ($x = 0$) and shows excellent agreement. In contrast, part (b) describes a spatial history, $\eta(x)$ at $t = 20$ s, in which comparisons between the BEM predictions and the Stokes 5th solution [18] identify a progressively increasing phase shift. Although this effect is small, it was unexpected and provoked an initial consideration of the drift velocity. With these calculations undertaken in a semi-Lagrangian frame, the nodal points are only allowed to move vertically. As a result, only the Eulerian return flow will be present within the calculations. For the prescribed wave conditions, Eq. (27) gives a value of $\bar{u}_{return} = -0.0082$ m s^{-1}. Superimposing this result on the Stokes 5th solution restores the excellent agreement with the BEM results (Fig. 7(b)).

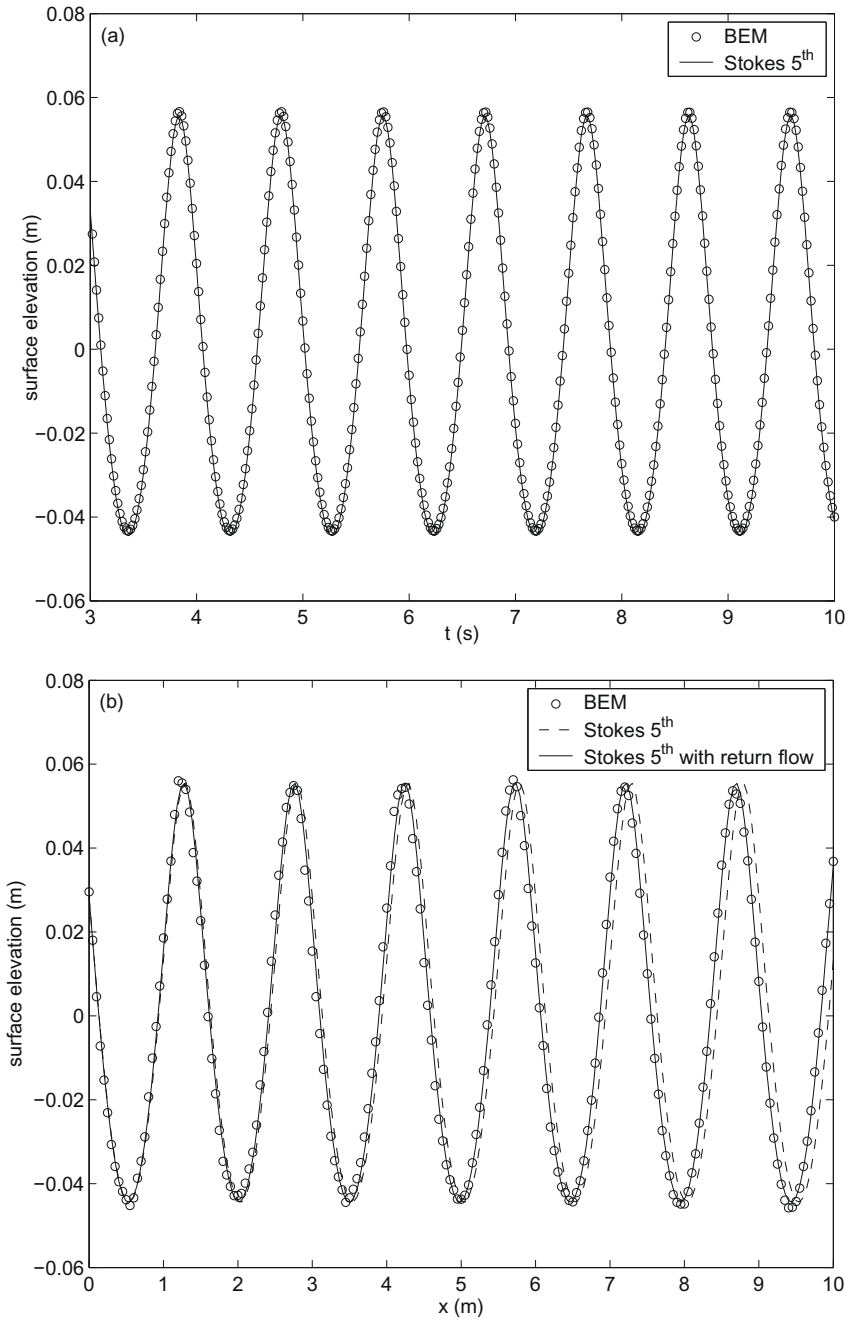

Fig. 7. Simulation of a regular wave train, $a = 0.05$ m, $\lambda = 1.5$ m. (a) $\eta(t)$ at $x = 0$, (b) $\eta(x)$ at $t = 20$ s.

This wave case is again considered in Fig. 8. Part (a) describes the spatial variation in the velocity potential on the water surface (ϕ on Γ_s) at $t = 20$ s; the input to the BEM calculations having again been specified as $\partial\phi/\partial n(t)$ on the boundary, Γ_l. Within the interval $0 < x < 10$ m the corresponding surface elevation data (Fig. 7(b)) confirms that a regular wave train has been established, whilst the surface potential (Fig. 8(a)) exhibits a mean (or wave-averaged) gradient corresponding to $\frac{\partial\bar{\phi}}{\partial x} = \bar{u}_{return} = 0.0088$ m s^{-1}. To further confirm this value Fig. 8(b) again concerns the spatial gradient of the potential on the water surface for exactly the same wave case. However, in this case the input to the wave model was given as a spatial description of the water surface elevation, $\eta(x)$ and the velocity potential $\phi(x)$ on that surface, both specified in terms of a Stokes 5th solution [18]. At either end of the input region, which describes some 12 wave cycles, the input values were tapered to zero. Within this set of calculations both the spatial discretisation and the time step were held constant, but the domain length was increased to 40 m to ensure that no wave motion could reach the corner points; the nodes located at

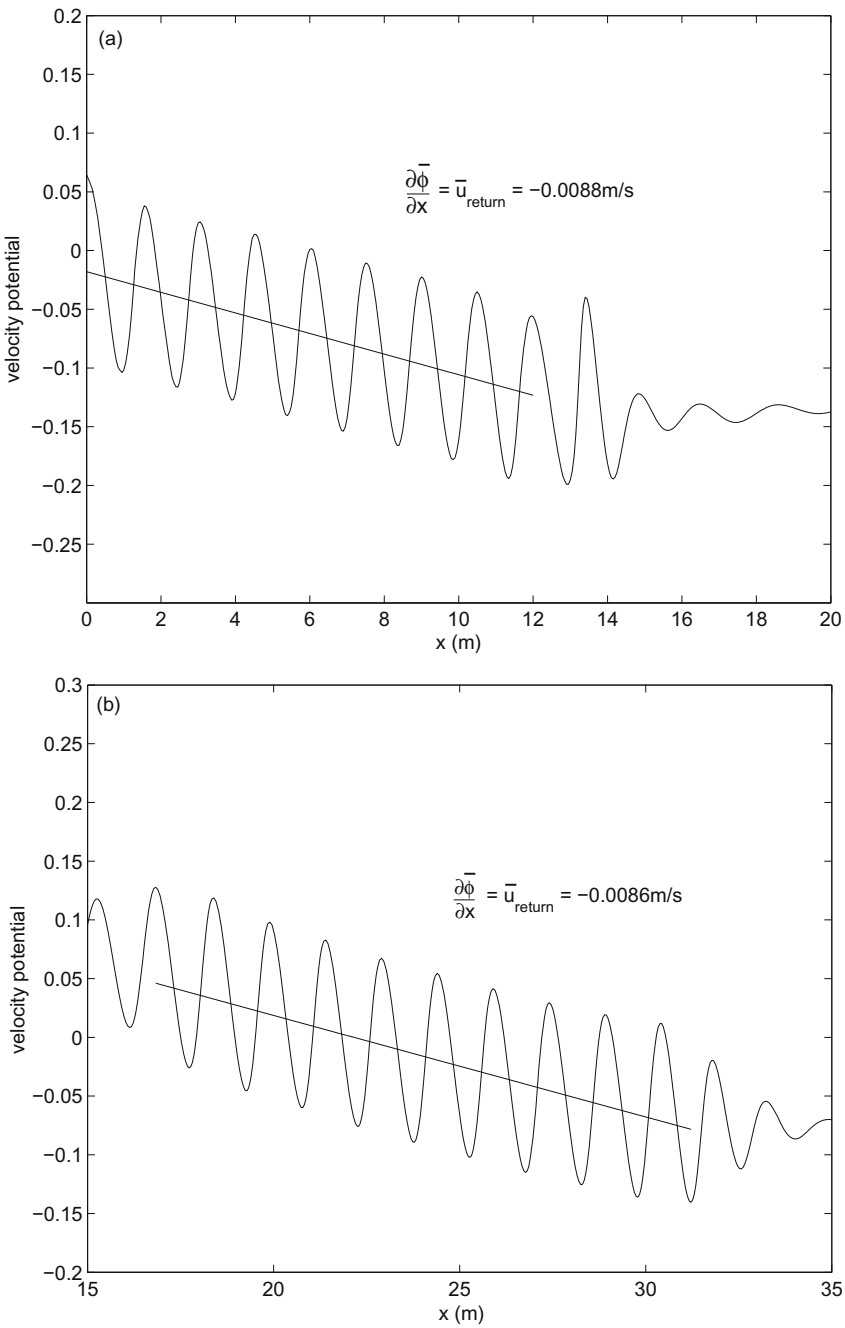

Fig. 8. Velocity potential of a regular wave train, $a = 0.05$ m, $\lambda = 1.5$ m. (a) $\phi(x)$ at $t = 20$ s, semi-Lagrangian calculations based on temporal input at $x = 0$ ($\bar{u}_{return} = -0.0088$ m s^{-1}). (b) $\phi(x)$ at $t = 20$ s, Lagrangian calculations based on spatial input at $t = 0$ ($\bar{u}_{return} = -0.0086$ m s^{-1}).

$x = 0$ and $x = 40$ m remaining at $z = 0$ throughout the calculations. This in turn ensured that the elements defining the corner points remained perpendicular, thereby eliminating any difficulties associated with the definition of the normal flux. Having time-marched the initial spatial conditions for 20 s in a fully Lagrangian sense, the surface potential achieved a (stable) wave averaged gradient of $\frac{\partial \bar{\phi}}{\partial x} = \bar{u}_{return} = 0.0086$ m s^{-1}. The agreement between these values (Fig. 8(a) and (b)) and their similarity to the second-order predicted value ($\bar{u}_{return} = 0.0082$ m s^{-1}) highlights the accuracy of the multiple flux method when utilised at the input corner.

Further evidence that the proposed model accurately simulates the mass transport velocity within the specified domain is provided by the total Lagrangian drift. By following the motion of one node through time (Fig. 9), the net drift of particles due to the motion of a wave train along the surface can be calculated as $\bar{u}_{drift} = 0.0599$ m s^{-1}. According to second-order theory,

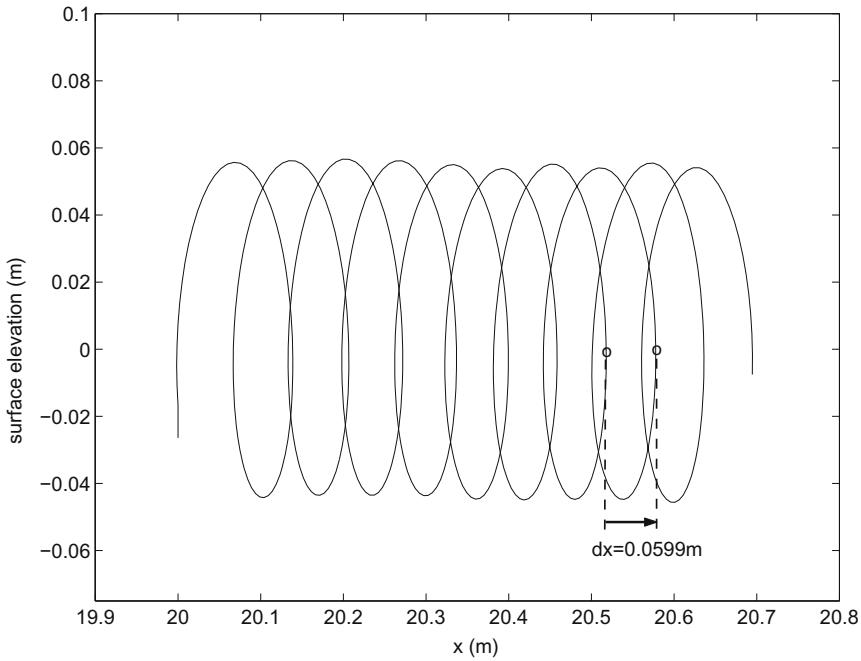

Fig. 9. Motion of a single node within the spatially input regular wave train ($a = 0.05$ m, $\lambda = 1.5$ m) as it propagates along the free surface.

Eq. (27), the predicted drift is $\bar{u}_{drift} = 0.0686 - 0.0082 = 0.0604$ m s^{-1}; the difference between this and the BEM calculations being less than 0.8%.

4.3. Transmission through an open sea corner

In this example, the ability of the downstream free surface corner to simulate the transmission of a regular wave through an open sea condition is assessed. The calculations were undertaken in a semi-Lagrangian frame, linear wave conditions were adopted ($a = 0.01$ m, $\lambda = 1$ m), and the numerical domain (including spatial discretisation and time step) was as described previously. However, no passive damping was implemented; the downstream boundary being specified as an open sea condition and modelled using the radiation condition specified in Eq. (23). To examine the behaviour of the corner node, the same wave case was also run in an identical domain, with the same discretisation, except it was of twice the length ($L_{long} = 40$ m). In this latter case the calculated wave properties at $x = 20$ m become independent of the end condition. Fig. 10 shows the time-history at the corner compared to the same x-position in the long domain case. It is clear that the agreement between these cases is excellent, highlighting the ability of the corner treatment to simulate the transmission of wave energy through an open sea condition.

4.4. Reflection of a solitary wave

This final example concerns the interactions between a unidirectional solitary wave and a vertical wall. This provides a further test of the model's ability to overcome the corner problem, not least because the largest surface elevation representing run-up arises at the corner point. This test case has the added advantage that the results of the numerical calculations can be directly compared to new laboratory studies undertaken in the Hydrodynamics Laboratory at Imperial College. These observations were undertaken in a wave flume of length 25 m, width 0.5 m and in a water depth of 0.5 m. Solitary waves were generated in the flume using a piston wavemaker located at the upstream end and allowed to propagate along the length of the flume before interacting with a solid, vertical wall at the downstream end. Although higher-order solitary wave theories exist (see, for example, Tanaka [19]), the first-order piston motion described by Goring [20] was adopted in the laboratory study. To ensure compatibility, the same first-order theory was also employed in the computations presented herein.

The free surface profile of a solitary wave is defined by

$$\eta(x,t) = H\mathrm{sech}^2(\kappa(x+\lambda-ct)), \tag{28}$$

where H is the height of the solitary wave generated on a water depth d and the quantities κ, c and λ are calculated according to

$$\kappa = \sqrt{\frac{3H}{4d^3}}, \tag{29}$$

$$c = \sqrt{g(d+H)}, \tag{30}$$

$$\lambda = \frac{l}{\kappa}, \tag{31}$$

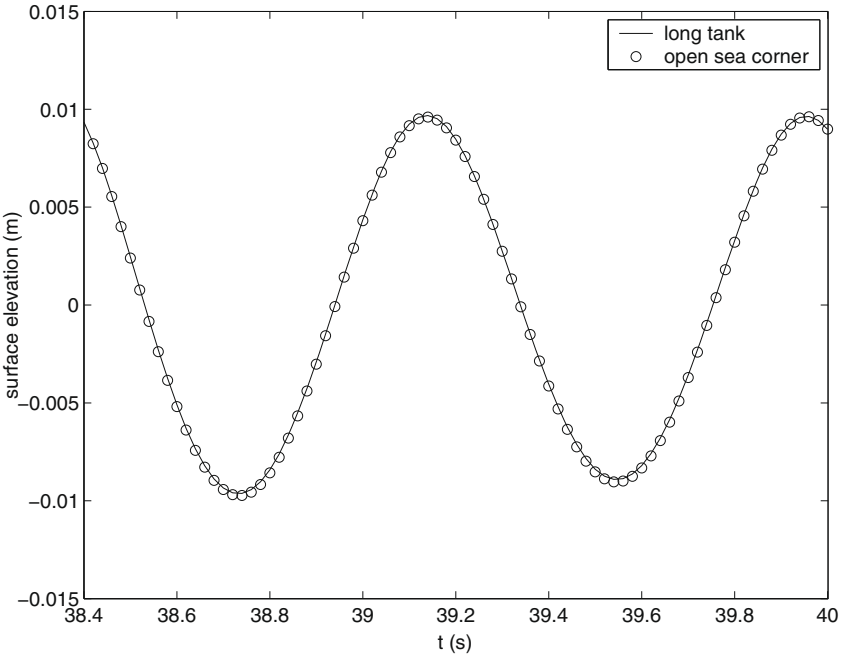

Fig. 10. Time-history of a regular wave train ($a = 0.01$ m, $\lambda = 1$ m) at an open sea corner compared to the same position in a domain of twice the length; the latter case being independent of the downstream boundary.

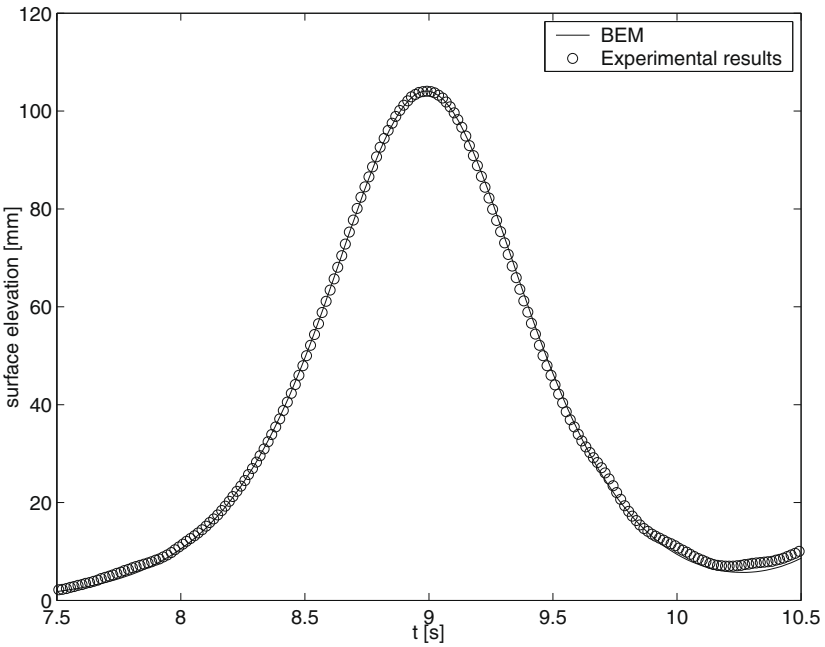

Fig. 11. Comparisons to laboratory data for the solitary wave example, ($H/d = 0.21$), showing the incident wave conditions 3 m from the wall.

the latter being the representative half-length of the solitary wave, with $l = (4-\epsilon)/(2\sqrt{\epsilon})$ and $\epsilon = 0.002$. To generate such a wave, Grilli and Horrillo [5] adopted the results of [20] and described the required horizontal position, $x_p(t)$, of a piston wave maker as satisfying

$$x_p(t) = \frac{H}{\kappa d}[\tanh(\kappa(ct - x_p(t) - \lambda)) + \tanh(\kappa\lambda)]. \tag{32}$$

This equation essentially describes the input to the wave paddle, although it should be noted that the appearance of x_p on both sides of the equation dictates an iterative solution. Following Goring [20], mass continuity requires that the velocity $u_p(t)$ of the piston motion at position $x_p(t)$ must satisfy

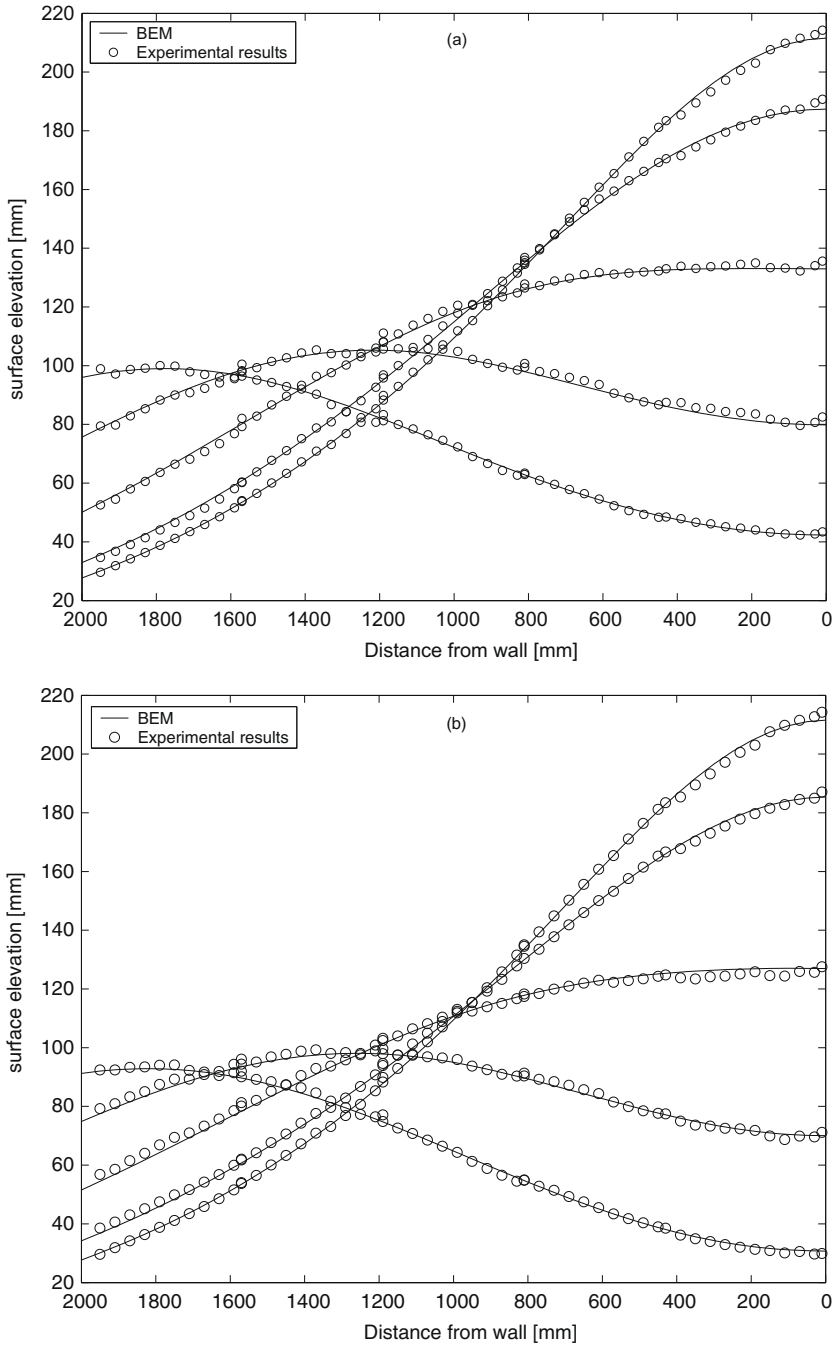

Fig. 12. Run-up and run-down of a solitary wave ($H/d = 0.21$) on a vertical wall, comparisons to laboratory data. (a) Run-up on the wall. The free surface is plotted at intervals of 0.2 s (10 time steps), leading up to the maximum run-up at the vertical wall which occurs at $t = 10.32$ s. (b) Run-down on the wall. Again the free surface is plotted at intervals of 0.2 s (10 time steps), beginning at the maximum run-up at the vertical wall which occurs at $t = 10.32$ s.

$$u_p(t) = \frac{c\eta}{\eta + d}. \tag{33}$$

Since the purpose of the physical piston is to mimic the fluid motion associated with a freely propagating solitary wave, the velocity associated with this motion is simply that of the fluid at $x_p(t)$. In the context of the numerical model, setting $x_p(t) = x_{input}$ where x_{input} is the fixed x-position of the input boundary, the input velocity $u_{input}(t)$ required for a semi-Lagrangian simulation of the BEM formulation described previously can be obtained by substituting equations (28) and (30) into (33), giving

$$u_{input}(t) = \frac{Hc}{d}\operatorname{sech}^2[\kappa(ct - x_{input} - \lambda) + H/d]. \tag{34}$$

Within the experimental study the effects of viscous dissipation and, to a lesser extent, nonlinearities in the nature of the paddle motion, lead to small discrepancies in the height of the solitary wave approaching the downstream boundary. To ensure that these effects did not invalidate the description of the solitary wave interacting with the vertical wall, the incident solitary wave profile was recorded 22 m downstream of the paddle (or 3 m upstream of the wall). This location was considered sufficiently close to the wall that no significant additional dissipation was likely to arise before the onset of wave reflection. At the same time, this location was sufficiently distant from the wall that most of the measured incident wave was unaffected by reflection; the latter only becoming significant in the tail of the wave. For the wave case presented herein, the non-dimensional wave height recorded at this reference gauge was $H/d = 0.21$, occurring in an effective water depth of $d = 0.494$ m.

The numerical domain was therefore defined as a closed tank of length $L = 20$ m and depth $d = 0.494$ m, with zero-flux conditions applied on both the bed and the reflective end wall. No numerical damping or radiation condition was applied, and a solitary wave was generated at the (fixed) vertical input boundary by specifying the boundary condition described in Eq. (34). Given the nature of a solitary wave this input velocity automatically ramps up smoothly from zero ensuring that the initial conditions are quiescent and allowing the computations to be undertaken from $t_0 = 0$ with the initial velocity potential specified as $\phi = 0$ on the free surface. The boundary of the numerical domain was discretised into 408 elements, with 200 of them placed on the free surface. Discretisation in space was therefore $\Delta x = 0.05$ m and $\Delta z = 0.06$ m, and the solution was time-marched with a time step of $\Delta t = 0.02$ s.

Figs. 11 and 12 contrast the laboratory observations and the numerical predictions for the solitary wave case noted above. Fig. 11 concerns a time-history of the water surface elevation recorded at the reference gauge located 3 m upstream of the wall (see above). This relates to the incident wave conditions, as far as the wave-wall interaction is concerned, and it is clear that the model provides a very good description of the laboratory observations. Fig. 12 provides a sequence of spatial profiles $\eta(\hat{x})$ for the solitary wave during (a) run-up and (b) run-down, where $\hat{x}$ defines the distance upstream of the vertical wall. In each plot five profiles are presented, corresponding to intervals of 0.2 s, showing the solitary wave interacting with the vertical wall. In both plots the uppermost trace (at $\hat{x} = 0$) corresponds to the maximum run-up arising at $t = 10.32$ s. On the basis of these comparisons the numerical model provides a good description of the measured data with no evidence of non-physical behaviour (local jetting) or errors at or near the corner node. Indeed, the only notable difference between the measured data and the numerical predictions occurs immediately adjacent to the wall, where the laboratory data exhibits a non-zero intersection angle due to highly localised viscous effects.

5. Concluding remarks

A fully nonlinear numerical model based on the Boundary Element Method (BEM) and appropriate to the description of free surface fluid flows has been introduced. Within the model the well-known difficulties associated with the corner problem have been tackled using the concept of multiple fluxes. This has not previously been applied in the context of a numerical wave tank and has been shown to be more accurate than other approaches currently applied; namely the use of discontinuous elements and the double node technique. In considering the latter, it is important to acknowledge that the extended compatibility conditions adopted in some recent formulations have not been considered. Indeed, on the basis of the present results, it is our assertion that the undoubted improvements in the double node models achieved using the extended compatibility conditions have only been required because of the inherent problems associated with the use of double nodes.

Examples have been presented in order to fully investigate the ability of the multiple flux corner treatment to simulate a variety of situations, including the motion of a standing wave inside a box, wave transmission through an input boundary and an open sea condition, and solitary wave reflection from a vertical wall. In all cases the behaviour at the domain corners was well predicted, highlighting the advantages of using the multiple flux approach for free surface simulations.

Throughout the paper much emphasis has been placed on the need to avoid smoothing, filtering and re-gridding. Whilst there are many problems where such an emphasis may be unnecessary, recent wave research [21,22] has shown that the unexpected occurrence of extreme waves may be related to highly localised and rapid changes in the wave spectrum. In both deep and shallow water wave cases this involves, at least in part, a transfer of energy to the higher frequencies. The extent of this transfer cannot be known *a priori* and, consequently, the imposition of smoothing, filtering or re-gridding may lead to the suppression of real energy shifts. Furthermore, in an engineering context, descriptions of the underlying water particle

kinematics are as important as accurate predictions of the water surface elevations. Unfortunately, the maximum kinematics (both velocities and accelerations) arise close to the water surface and are critically dependent upon both the spectral content of the sea state and the local curvature of the water surface, the two being closely related. If either or both are unduly influenced by applied numerical procedures, significant errors in the predicted kinematics will result. These topics will be the focus of future work, but in the context of Boundary Element modelling success will be closely related to an ability to overcome the corner problem. Similar arguments also apply to the study of wave-structure interactions, not least because the most interesting/critical information often relates to the fluid-structure interface and this corresponds to a corner position. The present results suggest that the implementation of multiple fluxes provides an accurate procedure with which to tackle such problems.

Acknowledgments

This work was undertaken as part of EPSRC grant GR/R64971 and the authors gratefully acknowledge this support. The authors also wish to thank Dr. Kenji Hamano for supplying his starting data for the Large Amplitude Standing Wave (LASW) simulation.

References

[1] M.S. Longuet-Higgins, E.D. Cokelet, The deformation of steep surface waves on water I. A numerical method of computation, Proceedings of the Royal Society of London, Series A (Mathematical and Physical Sciences) 350 (1660) (1976) 1–26.
[2] S.T. Grilli, J. Skourup, I.A. Svendsen, An efficient boundary element method for nonlinear water waves, Engineering Analysis with Boundary Elements 6 (2) (1989) 97–107.
[3] S.T. Grilli, I.A. Svendsen, Corner problems and global accuracy in the boundary element solution of nonlinear wave flows, Engineering Analysis with Boundary Elements 7 (4) (1990) 178–195.
[4] S. Grilli, R. Subramanya, Numerical modeling of wave breaking induced by fixed or moving boundaries, Computational Mechanics 17 (6) (1996) 374–391.
[5] S. Grilli, J. Horrillo, Numerical generation and absorption of fully nonlinear periodic waves, Journal of Engineering Mechanics – ASCE 123 (10) (1997) 1060–1069.
[6] C.A. Brebbia, J. Dominguez, Boundary Elements: An Introductory Course, second ed., Computational Mechanics Publications (McGraw-Hill), London, 1992.
[7] S. Ryu, M. Kim, P. Lynett, Fully nonlinear wave-current interactions and kinematics by a BEM-based numerical wave tank, Computational Mechanics 32 (2003) 336–346.
[8] W.J.D. Bateman, C. Swan, P.H. Taylor, On the efficient numerical simulation of directionally spread surface water waves, Journal of Computational Physics 174 (1) (2001) 277–305.
[9] S. Grilli, P. Guyenne, F. Dias, A fully non-linear model for three-dimensional overturning waves over an arbitrary bottom, International Journal for Numerical Methods in Fluids 35 (7) (2001) 829–867.
[10] C. Fochesato, F. Dias, S. Grilli, Wave energy focusing in a three-dimensional numerical wave tank, in: Proceedings of the Fifteenth International Offshore and Polar Engineering Conference, vol. 3, 2005, pp. 24–31.
[11] D. Otta, I. Svendsen, S. Grilli, Unsteady free surface waves in a region of arbitrary shape, Tech. Rep. 92-10, Center for Applied Coastal Research, University of Delaware, 1992.
[12] Y. Saad, M.H. Schultz, GMRES: a generalized minimum residual algorithm for solving nonsymmetric linear systems, SIAM Journal of Statistical and Scientific Computing 7 (3) (1986) 856–869.
[13] A. Clement, Coupling of two absorbing boundary conditions for 2D time-domain simulations of free surface gravity waves, Journal of Computational Physics 126 (1996) 139–151.
[14] K. Hamano, S. Murashige, K. Hayami, Boundary element simulation of large amplitude standing waves in vessels, Engineering Analysis with Boundary Elements 27 (6) (2003) 565–574.
[15] S. Baudic, A. Williams, A. Kareem, A two-dimensional numerical wave flume – Part 1: nonlinear wave generation, propagation, and absorption, Journal of Offshore Mechanics and Arctic Engineering 123 (2001) 70–75.
[16] R.G. Dean, R.A. Dalrymple, Water Wave Mechanics for Engineers and Scientists, World Scientific, 1995.
[17] J. Skourup, I. Jonsson, Computations of forces on, and particle orbits around, horizontal cylinders under steep waves, Ocean Engineering 19 (1992) 527–553.
[18] J. Fenton, A fifth-order stokes theory for steady waves, Journal of the Waterway Port Coastal and Ocean Engineering (ASCE) 111 (2) (1985) 216–234.
[19] M. Tanaka, The stability of solitary waves, Physics of Fluids 29 (3) (1986) 650–655.
[20] D. Goring, Tsunamis – the propagation of long waves onto a shelf, Tech. Rep. KH-R-38, Laboratory of Hydraulics & Water Resources, California Institute of Technology, 1978.
[21] T. Johannessen, C. Swan, On the nonlinear dynamics of wave groups produced by the focusing of surface-water waves, Proceedings of the Royal Society of London, Series A (Mathematical and Physical Sciences) 459 (2003) 1021–1052.
[22] R. Gibson, C. Swan, The evolution of large ocean waves: the role of local and rapid spectral changes, Proceedings of the Royal Society of London A 463 (2007) 21–48.